

# Graphene-on-Polymer Flexible Vaporizable Sensor

CNF Project Number: 1121-03

Principal Investigator(s): Amit Lal

User(s): Ved Gund

Affiliation(s): School of Electrical and Computer Engineering, Cornell University

Primary Source(s) of Research Funding: NSF-EFRI

Contact(s): amit.lal@cornell.edu, vvg3@cornell.edu

Website: <http://www.sonicmems.ece.cornell.edu/>

Primary CNF Tools Used: GSI PECVD, CVC SC4500 odd-hour evaporator, Oxford 81, Unaxis DRIE, spinners, SÜSS MA-6, Zeiss SEM

## Abstract:

Wireless sensor nodes integrated on flexible substrates are critical to meet the demands of a burgeoning market of wearable sensors, fieldable environmental sensors, and consumer electronics for Internet-of-Things (IoT) applications. While silicon-based circuits are pervasive, they face critical challenges for the aforementioned new and emerging applications. Wearable sensors necessitate conformality and stretchability to curved surfaces, in contrast to silicon-based sensors which are non-compliant. The use of silicon substrates for sensor nodes in a large, distributed network of sensors, whether for diagnostic and therapeutic biomedical devices or for soil and crop monitoring, also poses a significant concern from a sustainability standpoint since these sensors cannot be reacquired or resorbed easily back into the natural environment which can lead to non-degradable waste accumulation. Hence, it is critical to design sensors and electronics on flexible substrates that can also incorporate mechanisms for vaporization or disintegration which would minimize electronic waste. With this perspective, we have developed a graphene-on-polymer vaporizable and flexible piezoresistive sensor platform. This sensor technology can be used for wearable microsystems and disposable environmental sensors. A proof-of-concept pressure sensor with a high sensitivity of  $68 \times 10^{-3} \text{ kPa}^{-1}$  has been demonstrated. The device needs 22 mW to achieve a temperature of  $220^\circ\text{C}$  for the partial vaporization of a  $1 \text{ mm}^2$  membrane made of  $1.8 \mu\text{m}$  thick polypropylene carbonate (PPC), thus demonstrating a pathway to sensor self-destruction.

## Summary of Research:

It is essential to design flexible sensors with materials that have high mechanical strength for stretchability and conformality as well as excellent electronic properties. Atomically thin two-dimensional graphene is an outstanding candidate for such sensors because of its high Young's modulus of 1 TPa and as zero-bandgap semi-metal with out-of-plane p-orbital electrons for conduction modulation [1]. These properties make it suitable for piezoresistive sensing. Flexible graphene-based piezoresistive sensors with record high sensitivities have previously been reported [2]. Our work (schematic in Figure 1) demonstrates a graphene-on-polymer flexible piezoresistive pressure sensor that uses lithographically defined metal electrodes and membranes while maintaining a high quality of graphene as the piezoresistive sensor. The PPC is a highly compliant and flexible structural layer (Young's modulus of 1 GPa) for the sensor with low-temperature vaporization for potential self-destruction on environmental resorption [3].

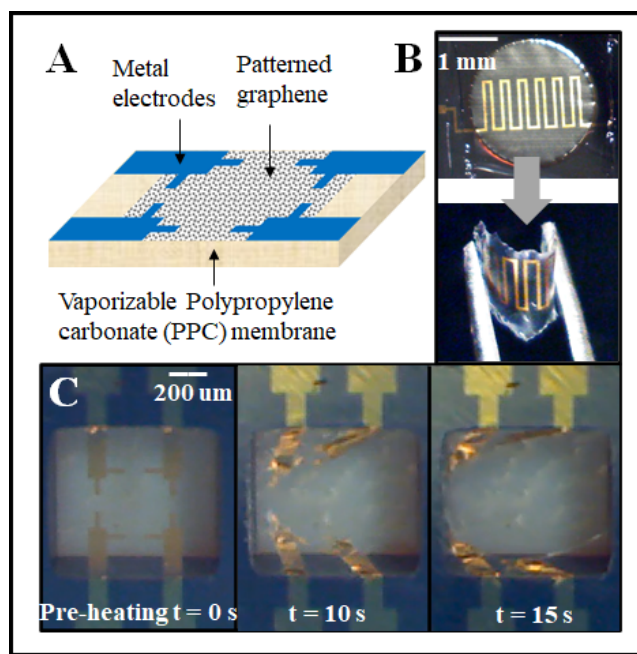


Figure 1: A) Flexible vaporizable pressure sensor architecture with lithographically defined graphene and metal electrodes on PPC. B) Flexibility: Metal-on-PPC piezoresistor on Si wafer (top) and after scribing out and bending with tweezers (bottom) C) Vaporization: Time series of sensor transience by vaporization of PPC in 15 seconds.

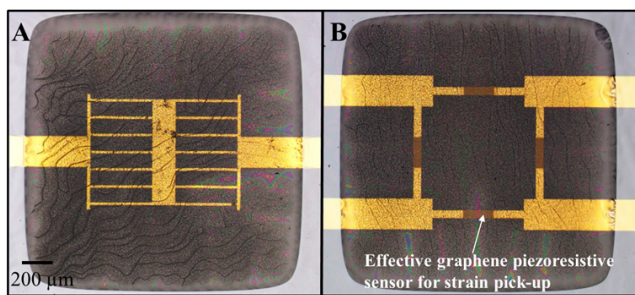


Figure 2: Optical micrographs of (A) Ti/Au metal-on-PPC flexible sensor and (B) graphene-on-PPC with false color between metal electrodes to show the effective graphene pressure sensing region for strain pick-up.

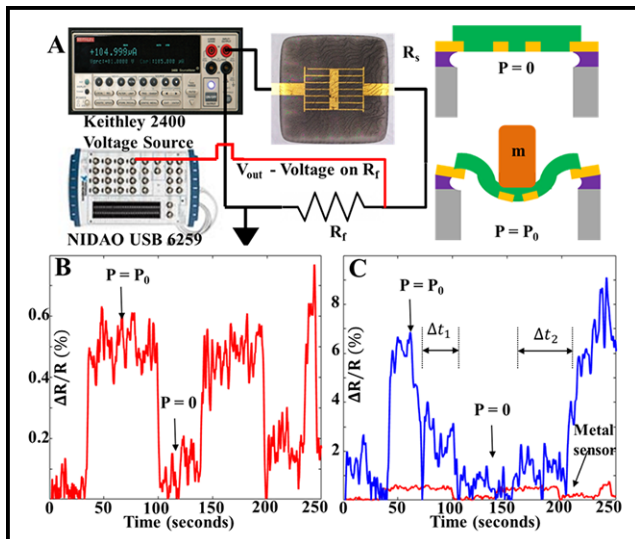


Figure 3: A) Piezoresistive pressure sensor test-setup. B) Fractional change in resistance ( $\Delta R/R$ ) for the metal sensor and C) Graphene sensor for loading and unloading of pressure  $P_0$ . The graphene sensor shows delays in response to unloading and loading after the first cycle.

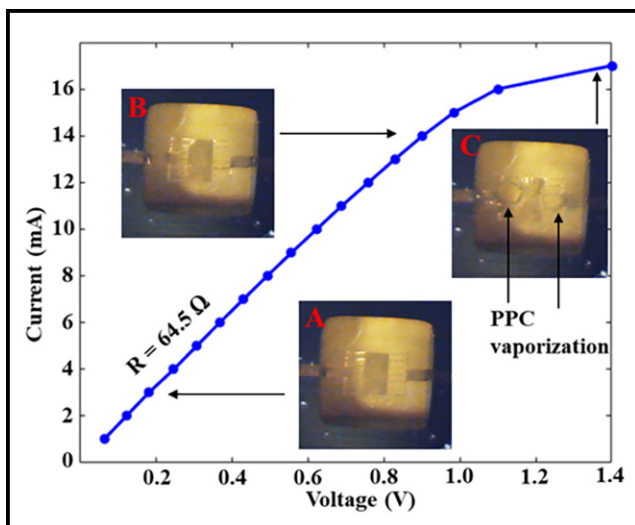


Figure 4: Voltage generated on the sense resistor vs. input current. A) For low input power  $< 15$  mW, the sensor remains intact. B) As the input is increased further, the sensor starts to vaporize. C) Partial vaporization at sensor end-of-life occurs before the resistor breaks, producing an open circuit.

## Fabrication:

$0.5 \mu\text{m}$  and  $1 \mu\text{m}$  PECVD oxide ( $\text{SiO}_2$ ) films were deposited on the device side and backside respectively of a  $500 \mu\text{m}$  silicon wafer with the GSI PECVD tool. PECVD oxide on the backside of the wafer was then patterned by reactive etching in the Oxford 81 tool followed by deep silicon etching in the Unaxis DRIE tool to produce oxide membranes on the device side.  $10 \text{nm}/40 \text{nm}$  Ti/Au was evaporated on the  $0.5 \mu\text{m}$  device side and patterned with lift-off to realize metal contacts to the piezoresistive graphene layer using the odd-hour evaporator. Commercially purchased CVD-grown single layer graphene (SLG) on copper foil was then transferred on the device side with PMMA as a handle layer and patterned with oxygen plasma in the Oxford 81 to confine it to the membrane region. A 5 wt. % PPC solution in dichloromethane (DCM) was then spin-coated on the device side to produce a  $1.8 \mu\text{m}$  PPC film, which eventually serves as the sensor membrane — details of the PPC solution preparation are available in [4]. The graphene-on-polymer and metal-on-polymer devices are shown in Figure 2. Figure 3 shows the electrical configuration for testing the metal-on-polymer and graphene-on-polymer devices with sensitivities of  $6.12 \times 10^{-3}$  and  $68 \times 10^{-3} \text{ kPa}^{-1}$  respectively, the graphene sensor showing a more than 10x improvement in performance over the metal strain gauge. Figure 4 shows the DC current vs voltage (IV) sweep and corresponding sensor self-destruction with optical verification.

## Conclusions and Future Steps:

Our work demonstrates a graphene-on-polymer flexible sensor architecture for self-destructing electronics with low-voltage operation and high pressure-sensitivity using a representative sensor device. The architecture can be extended other self-destructing sensors such as accelerometers, gyroscopes, and gas sensors for a more ubiquitous self-destructing sensor platform.

## References:

- [1] H. Tian, et al., "A graphene-based resistive pressure sensor with record-high sensitivity in a wide pressure range," *Sci. Rep.*, vol. 5, no. 1, pp. 1-6, Feb. 2015.
- [2] P. Miao, J. Wang, C. Zhang, M. Sun, S. Cheng, and H. Liu, "Graphene Nanostructure-Based Tactile Sensors for Electronic Skin Applications," *Nano-Micro Letters*, vol. 11, no. 1. SpringerOpen, Sep. 01, 2019.
- [3] V. Gund and A. Lal, "Graphene-On-Polymer Flexible Vaporizable Sensor," in *Proceedings of the IEEE International Conference on Micro Electro Mechanical Systems (MEMS)*, Jan. 2021, vol. 2021-January, pp. 521-524.
- [4] V. Gund, A. Ruyack, A. Leonardi, K. B. Vinayakumar, C. Ober, and A. Lal, "Spatially Controlled Transience of Graphene-Polymer Electronics with Silicon Singulation," *Adv. Funct. Mater.*, vol. 29, no. 20, p. 1900592, May 2019.

# Towards Low-Coercive Field Operation of Sputtered Ferroelectric $\text{Sc}_x\text{Al}_{1-x}\text{N}$

CNF Project Number: 1122-03

Principal Investigator(s): Amit Lal

User(s): Ved Gund, Benyamin Davaji

Affiliation(s): School of Electrical and Computer Engineering, Cornell University

Primary Source(s) of Research Funding: Defense Advanced Research Projects Agency (DARPA)

Contact(s): amit.lal@cornell.edu, vvg3@cornell.edu

Website: <http://www.sonicmems.ece.cornell.edu/>

Primary CNF Tools Used: AJA sputter deposition, AJA ion mill, PT770, Oxford PECVD, SEM

## Abstract:

This work reports on the ferroelectric properties of scandium aluminum nitride ( $\text{Sc}_x\text{Al}_{1-x}\text{N}$ ) thin films with an Sc-concentration between 22-30%. The goal of this work is to engineer a low coercive field in  $\text{Sc}_x\text{Al}_{1-x}\text{N}$  for low-voltage post-CMOS compatible RF frontends. Films between 200 and 300 nm  $\text{Sc}_x\text{Al}_{1-x}\text{N}$  were deposited on platinum (Pt) and molybdenum (Mo) electrodes. Lateral and vertical capacitors were tested over a range of electric fields, frequencies, and electrode sizes. Measured coercive field ( $E_C$ ) and remnant polarization ( $P_r$ ) values were between 3.9-6.2 MV/cm and 58-170  $\mu\text{C}/\text{cm}^2$ . Frequency, temperature, and device area-dependence were studied to identify trends towards low coercive field operation of the material. An anomalous observation relating Sc-concentration and film stress, with  $E_C$  and  $P_r$  is reported to present prospects for decoupled tuning knobs to engineer lowered  $E_C$  in  $\text{Sc}_x\text{Al}_{1-x}\text{N}$ .

## Summary of Research:

Aluminum nitride (AlN) is the material of choice for MEMS RF resonators due to its excellent piezoelectric properties and CMOS compatibility. Fundamental limits in the piezoelectric properties of AlN have inspired the exploration of alloys of AlN towards enhanced piezoelectric properties. One such alloy is scandium aluminum nitride ( $\text{Sc}_x\text{Al}_{1-x}\text{N}$ ), which presents a tuning mechanism to increase the piezoelectric coefficient by  $\sim 4x$  with scandium incorporation. Theoretical calculations predict that monotonically increasing Sc-concentration can decrease the energy barrier between the parent wurtzite structure and the hexagonal phase in  $\text{Sc}_x\text{Al}_{1-x}\text{N}$  to produce ferroelectric switching. The recent discovery of ferroelectric switching in high Sc-concentration  $\text{Sc}_x\text{Al}_{1-x}\text{N}$  ( $x > 0.27$ ), has confirmed these predictions and generated significant interest as the first III-V ferroelectric [1]. Ferroelectricity has been demonstrated with Sc-concentration as low as 10%, and  $\text{Sc}_x\text{Al}_{1-x}\text{N}$  has been used for ferroelectric resonators [2,3]. A major challenge to use  $\text{Sc}_x\text{Al}_{1-x}\text{N}$  for device applications is the requirement for high on-chip voltages ( $>100\text{V}$ ) due to its high  $E_C$ . Here, we present results that map the design space of parameters which present a pathway towards lower  $E_C$  in  $\text{Sc}_x\text{Al}_{1-x}\text{N}$  [4,5].

**Fabrication.** Multiple film stacks were made for testing the impact of bottom electrode and substrate on  $\text{Sc}_x\text{Al}_{1-x}\text{N}$ . Ti/Pt was deposited on blanket silicon in the AJA sputtering

tool followed by  $\text{Sc}_x\text{Al}_{1-x}\text{N}/\text{Mo}$  deposition at an external vendor (OEM). In another variation,  $\text{SiO}_2$  was deposited in the Oxford PECVD followed by  $\text{Mo}/\text{Sc}_x\text{Al}_{1-x}\text{N}/\text{Mo}$  deposition at OEM. The film stacks were deposited in a cluster-line tool followed by etching of the top Mo and  $\text{Sc}_x\text{Al}_{1-x}\text{N}$  in the PT770 etcher. For the bottom electrode, Ti/Pt was etched in the AJA ion mill whereas the Mo was etched in the PT770. For etch-calibration, AlN films were deposited in the OEM Endeavor M1 and etched in the PT770.

**Results.** A setup with continuous wave positive-up-negative-down (PUND) was used for ferroelectric testing of  $\text{Sc}_x\text{Al}_{1-x}\text{N}$  (Figure 1A). The P and N pulses include both switching and leakage currents. The U and D pulses include only the leakage and can be subtracted from P and N pulses respectively to get the switching current (Figure 1B). Representative polarization vs. E-field (PE) loops are shown in Figure 1C.

*In situ* heating of capacitors on 300 nm  $\text{Sc}_{0.30}\text{Al}_{0.70}\text{N}$  shows a monotonic decrease in  $E_C$  without a significant change in  $P_r$  (Figure 2A). The temperature coefficient of  $E_C$  for this sample is  $\sim 8.8 \text{ kV}/^\circ\text{C}$  (Figure 2B). Figure 3 shows the area and frequency-dependence of  $E_C$  and  $P_r$  across a range of electrode sizes and frequencies from 20-100  $\mu\text{m}$  diameter and 1-8 kHz.  $E_C$  increases with an increase in

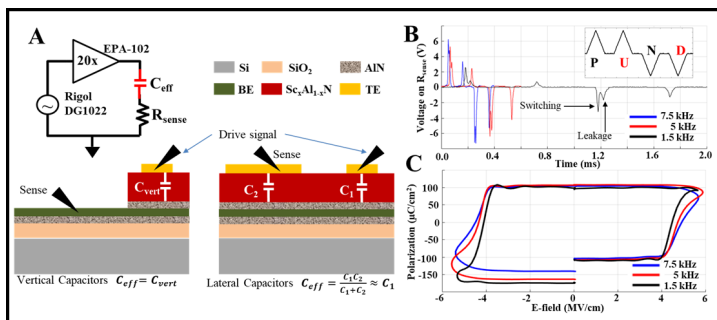


Figure 1: A) Modified Sawyer-Tower circuit for testing ferroelectric ScAlN capacitors and probing configurations for testing vertical and lateral configurations. B) Raw output voltage waveforms at various switching frequencies for PUND test (generic input waveform inset) C) Polarization vs. E-field (PE) loops generated by integrating switching currents from B.

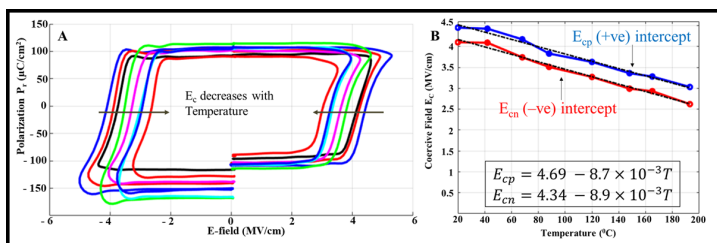


Figure 2: A) Polarization vs. E-field (PE) loops for 40  $\mu\text{m}$  capacitor on 300 nm  $\text{Sc}_{0.30}\text{Al}_{0.70}\text{N}$  between RT and 195 $^{\circ}\text{C}$ . B) Linear decrease in  $E_c$  with increase in temperature with a coefficient of  $\sim 8.8$  kV/cm/ $^{\circ}\text{C}$ .

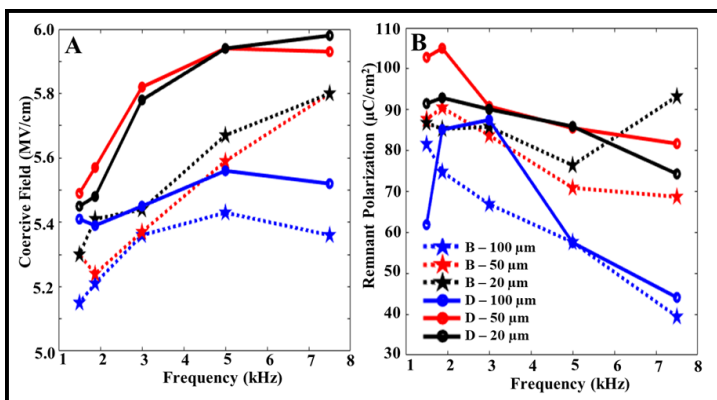


Figure 3: Plots of A)  $E_c$  and B)  $P_r$  versus frequency for capacitors of 20-100  $\mu\text{m}$  diameter with Sc-concentration of 30% and 22% on Mo and Pt electrodes to map frequency and area-dependence of ferroelectricity.

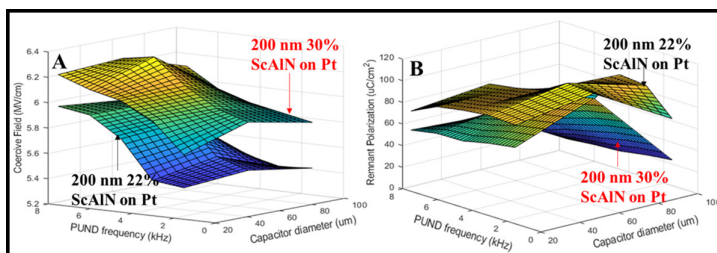


Figure 4: 3D map of A)  $E_c$  and B)  $P_r$  for 30% and 22% ScAlN on Pt electrodes tested over the range of capacitor sizes and frequencies. The 22% ScAlN has lower  $E_c$  and higher  $P_r$  due to a favorable tensile film stress of 102 MPa.

frequency and decreases with an increase in electrode size because a larger capacitor has more domains for ferroelectric switching and a lower frequency allows for more complete switching.  $P_r$  decreases with an increase in electrode size due to higher leakage in larger devices.

Figure 4 shows an anomalous dependence of  $E_c$  on Sc-concentration across a range of electrode sizes and frequencies — a lower Sc-concentration shows lower  $E_c$  due to a favorable tensile stress of 102 MPa compared to a compressive stress of 80 MPa. This stress-control shows a path towards decoupled knobs for tuning ferroelectricity, other than Sc-concentration.

## Conclusions and Future Steps:

Our work maps out the design space of low  $E_c$ -operation (as low as 2.5 MV/cm) in  $\text{Sc}_x\text{Al}_{1-x}\text{N}$  with *in situ* heating, and high frequency operation.

The use of this low  $E_c$  in ferroelectric transistors, resonators, transducers, and NEMS devices is the subject of on-going research.

## References:

- [1] S. Fichtner, N. Wolff, F. Lofink, L. Kienle, and B. Wagner, "AlScN: A III-V semiconductor based ferroelectric," *Journal of Applied Physics*, 2019.
- [2] S. Yasuoka, et al., "Effects of deposition conditions on the ferroelectric properties of ( $\text{Al}_{1-x}\text{Sc}_x\text{N}$ ) thin films," *Journal of Applied Physics*, 2020.
- [3] J. Wang, M. Park, S. Mertin, T. Pensala, F. Ayazi, and A. Ansari, "A Film Bulk Acoustic Resonator Based on Ferroelectric Aluminum Scandium Nitride Films," *Journal of Microelectromechanical Systems*, 2020.
- [4] V. Gund, et al., "Temperature-dependent Lowering of Coercive Field in 300 nm Sputtered Ferroelectric  $\text{Al}_{0.70}\text{Sc}_{0.30}\text{N}$ ," *IEEE ISAF*, 2021.
- [5] V. Gund, et al., "Towards Realizing the Low-Coercive Field Operation of Sputtered Ferroelectric  $\text{Sc}_x\text{Al}_{1-x}\text{N}$ ," *TRANSDUCERS 2021- 21st Int. Conf. Solid-State Sensors, Actuators Microsystems*, 2021.

# A High-Performance Epitaxial Transparent Oxide Thin-Film Transistor Fabricated at Back-End-Of-Line Temperature ( $< 450^{\circ}\text{C}$ ) by Suboxide Molecular-Beam Epitaxy

CNF Project Number: 2543-17

Principal Investigator(s): Darrell Schlom

User(s): Jisung Park

Affiliation(s): Department of Material Science and Engineering, Cornell University, Ithaca, NY 14853, USA

Primary Source(s) of Research Funding: Semiconductor Research Corporation

Contact(s): schlom@cornell.edu, gp359@cornell.edu

Primary CNF Tools Used: PT720/740, PVD75 sputter deposition, Autostep i-line stepper

## Abstract:

We fabricated a micron-scale field effect transistor (FET) based on epitaxial  $\text{In}_2\text{O}_3$  thin film with drain current of 0.2 A/mm and on-off ratio of  $1 \times 10^8$  at room temperature. The whole device manufacturing process including epitaxial  $\text{In}_2\text{O}_3$  growth takes place below  $450^{\circ}\text{C}$ , making it suitable for back-end-of-line (BEOL) process.

## Summary of Research:

Epitaxial layer of indium oxide ( $\text{In}_2\text{O}_3$ ) was formed below the threshold for BEOL process,  $T_{\text{sub}} < 450^{\circ}\text{C}$ , with narrow rocking curve less than  $0.05^{\circ}$  and low surface roughness of 0.45 nm RMS value, using recently developed version of molecular-beam epitaxy called suboxide MBE [1,2]. At lower carrier concentration regime, an epitaxial  $\text{In}_2\text{O}_3$  film attained a mobility of  $28 \text{ cm}^2\text{V}^{-1}\text{s}^{-1}$  at a carrier concentration of  $1.35 \times 10^{19} \text{ cm}^{-3}$ . We chose this film to make a FET device because of its low carrier concentration, which is ideal for achieving complete depletion.

We used reactive ion etching using the same conditions we described recently for etching stannate materials for device isolation, and it worked well for  $\text{In}_2\text{O}_3$  [3]. Contacts at the source/drain and top gate were made with sputtered ITO thin film. For dielectric, ALD-grown  $\text{HfO}_2$  was deposited. Figure 1 depicts the device schematic. The characteristics of the devices are shown in Figure 2 and Figure 3.

The hysteresis behavior in the transfer characteristic with respect to the voltage sweep directions is similar to what we saw on  $\text{BaSnO}_3$ -based field effect transistor made with the same technique. It is believed this non-ideal behavior is attributed to the defects in  $\text{HfO}_2$ . The drain current of the device in the output characteristic is 0.2 A/mm and the on-off ratio is  $1 \times 10^8$ . In Figure 4, we compared the results of our devices to those of the most advanced oxide channel thin film transistor [4-49].

Our result is in the upper left corner, where the expected performance with high drain current and on-off ratio should be found. This indicates that our results are comparable to the best-performing devices based on alternative oxide channel materials, and thus promising.

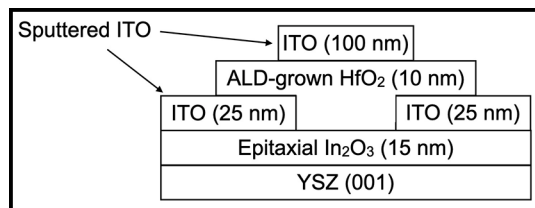


Figure 1: Device schematic.

## References:

- [1] P. Vogt, et al., APL Materials 9 (2021) 031101.
- [2] P. Vogt and O. Bierwagen, Phys. Rev. Mat. 2 (2018) 120401.
- [3] J. Park, US Patent 10,868,191 (2020).
- [4] Z. Yuan, et al., Thin Solid Films 519, 3254-3258 (2011).
- [5] P. K. Nayak, et al., Appl. Phys. Lett. 103, 033518 (2013).
- [6] N. Mitoma, et al., Appl. Phys. Lett. 104, 102103 (2014).
- [7] L. Wang, et al., 2020 IEEE Symposium on VLSI Technology (2020).
- [8] M. Si, et al., IEEE Trans. Electron Devices 68, 1075-1080 (2021).
- [9] M. Si, et al., IEEE Electron Device Lett. 42, 184 (2021).
- [10] M. Si, et al., Nano Lett. 21, 500-506 (2021).
- [11] J. Park, et al., APL Mater. 8, 011110 (2020).
- [12] U. Kim, et al., APL Mater. 3, 036101 (2015).
- [13] J. Shin, et al., Appl. Phys. Lett. 109, 262102 (2016).
- [14] C. Park, et al., Appl. Phys. Lett. 105, 203503 (2014).
- [15] Y. M. Kim, et al., APL Mater. 5, 016104 (2017).
- [16] Y. M. Kim, et al., Appl. Phys. Exp. 9, 011201 (2016).
- [17] Y. Kim, et al., APL Mater. 6, 096104 (2018).
- [18] J. Cheng, et al., J. Vac. Sci. Technol. B 38, 012201 (2020).
- [19] J. Cheng, et al., IEEE Electron Device Lett. 41, 621 (2020).
- [20] J. Cheng, et al., Appl. Phys. Lett. 118, 042105 (2021).
- [21] H.-H. Hsieh and C.-C. Wu, Appl. Phys. Lett. 89, 041109 (2006).
- [22] E. Fortunato, et al., Adv. Mater. 24, 2945-2986 (2012).
- [23] B. Bayraktaroglu, et al., IEEE Electron Device Lett. 30, 946-948 (2009).
- [24] B.-Y. Oh, et al., Semicond. Sci. Technol. 26, 085007 (2011).
- [25] B. Bayraktaroglu, et al., IEEE Electron Device Lett. 29, 1024-1026 (2008).
- [26] K. Nomura, et al., Science 300, 1269-1272 (2003).
- [27] K. Nomura, et al., Nature 432, 488-492 (2004).
- [28] R. Yao, et al., Appl. Phys. Lett. 112, 103503 (2018).
- [29] N. C. Su, et al., IEEE Electron Device Lett. 30, 1317-1319 (2009).
- [30] C.-Y. Chung, et al., Appl. Phys. Lett. 106, 123506 (2015) /igzo.
- [31] I. Noviyana, et al., Materials 10, 702 (2017).
- [32] S. Tomai, et al., Jpn. J. Appl. Phys. 51, 03CB01 (2012).
- [33] R. Jany, et al., Adv. Mater. Int. 1, 1300031 (2013).
- [34] L. Dong, et al., Proc. IEEE Int. Electron Devices Mtg, 26.4.1-26.4.4. (2010).
- [35] H. Zhou, et al., Appl. Phys. Lett. 111, 092102 (2017).
- [36] A. J. Green, et al., IEEE Electron Device Lett. 38, 790-793 (2017).
- [37] Z. Xia, et al., IEEE Electron Device Lett. 39, 568-571 (2018).
- [38] N. Moser, et al., IEEE Electron Device Lett. 38, 775-778 (2017).
- [39] K. D. Chabak, et al., IEEE Electron Device Lett. 39, 67-69 (2018).
- [40] H. Zhou, et al., ACS Omega 2, 7723.7729 (2017).
- [41] N. A. Moser, et al., Appl. Phys. Lett. 110, 143505 (2017).
- [42] W. S. Hwang, et al., Appl. Phys. Lett. 104, 203111 (2014).
- [43] C. Ju, et al., Curr. Appl. Phys. 16, 300-304 (2016).
- [44] R. E. Presley, et al., J. Phys. D: Appl. Phys. 37, 2810-2813 (2004).
- [45] S. Li, et al., Nat. Mater. 18, 1091-1097 (2019).
- [46] M. Si, et al., ACS Nano 14, 11542-11547 (2020).
- [47] J. Zhang, et al., IEEE Electron Device Lett. 40, 1463 (2019).
- [48] A. Verma, et al., Appl. Phys. Lett. 105, 113512 (2014).
- [49] H. Chandrasekar, et al., ACS Appl. Electron. Mater. 2, 510.516 (2020).

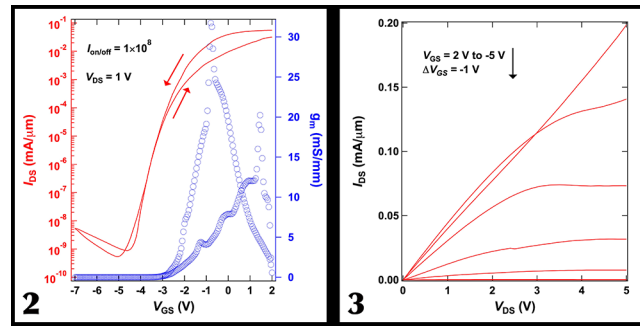


Figure 2, left: Transfer characteristic of the device. Figure 3, right: Output characteristic of the device.

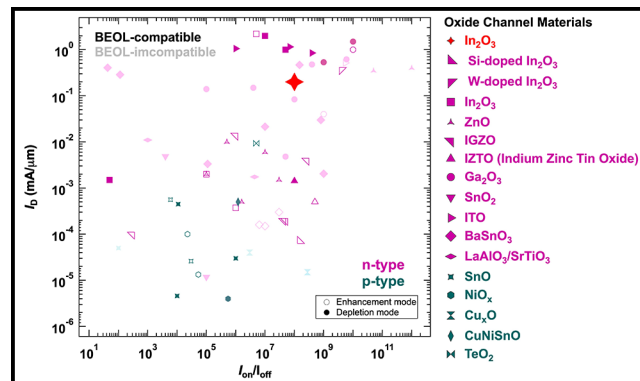


Figure 4: The comparison of device performances based on oxide channel materials in terms of drain current and on-off ratio.

# Fabrication and Manipulation of Microscale Opto-Electrically Transduced Electrodes (MOTEs)

CNF Project Number(s): 2578-17, 2836-19

Principal Investigator(s): Prof. Alyosha C. Molnar

User(s): Sunwoo Lee, Sanaz Sadeghi, Shahab Ghajari, Devesh Khilwani

Affiliation(s): Electrical and Computer Engineering, Cornell University

Primary Source(s) of Research Funding: National Institutes of Health (NIH)

Contact(s): am699@cornell.edu, sl933@cornell.edu, ss3842@cornell.edu, sg2367@cornell.edu, dk842@cornell.edu

Website: <https://molnargroup.ece.cornell.edu/>

Primary CNF Tools Used: ABM contact aligner, AJA sputter deposition, Westbond 7400A ultrasonic wire bonder, Oxford 100, Oxford 81, Oxford 82, Unaxis deep Si etcher, Oxford PECVD, Oxford ALD, Anatech, P7 profilometer, ZEISS Ultra and Supra SEMs

## Abstract:

Recording neural activity in live animals *in vivo* is critical in elucidating how the brain functions. However, such recording poses several challenges. Electrical techniques typically require electrodes to be tethered to the outside world directly via a wire, or indirectly via an RF Coil [1], which is much larger than the electrodes themselves. Tethered implants suffer from the residual motions between electrodes and neurons as the brain moves, limiting our ability to measure from peripheral nerves in moving animals, especially in smaller organisms such as zebra fish or fruit flies. On the other hand, optical techniques, which are becoming increasingly potent, are often limited to subsets of neurons in any given organism, impeded by scattering of the excitation light and emitted fluorescence, and limited to low temporal resolution [2]. Here we present an untethered opto-electrical system on chip (SoC), Micro-scale Opto-electrically Transduced Electrodes (MOTEs), which are powered by, and communicating through a microscale optical interface, combining many benefits of optical techniques with high temporal-resolution of electrical recording.

## Summary of Research:

Our fabrication starts with about 5 mm × 5 mm, conventional 180 nm complementary metal oxide semiconductor (CMOS) die, which contains the electronics for signal amplification, encoding, and transmission. The CMOS die is then integrated with AlGaAs diode, which acts as a photo-voltaic (PV) as well as light emitting diode (LED), hence the diode is abbreviated as PVLED. The PVLED provides an optical link which powers the electronics and transmits encoded signals in optical pulses. The MOTE utilizes pulse position modulation (PPM) for signal encoding for its high information-per-photon efficiency, where the spacing between the output pulses is proportional to the measured electric field of neuronal signals across the measurement electrodes. Figure 1 depicts a conceptual deployment and system description of such MOTE [3].

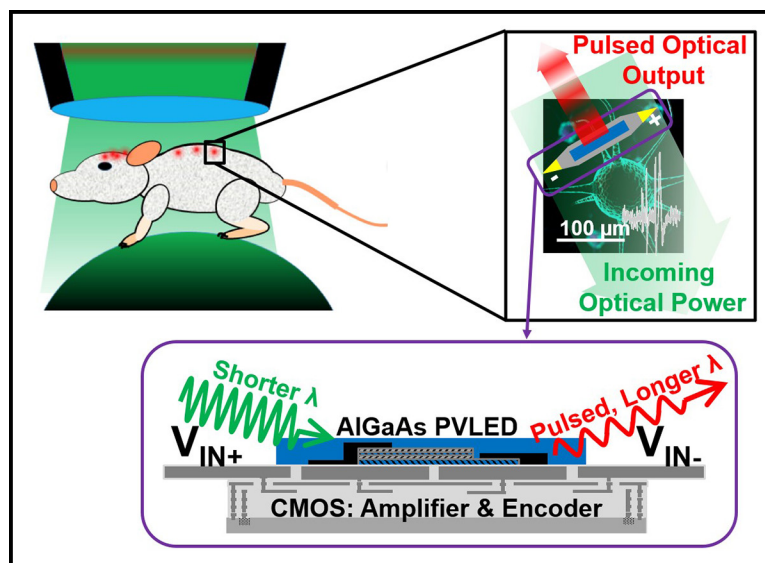


Figure 1: An exemplary implementation and system level description of the MOTEs in a mouse animal model [3].

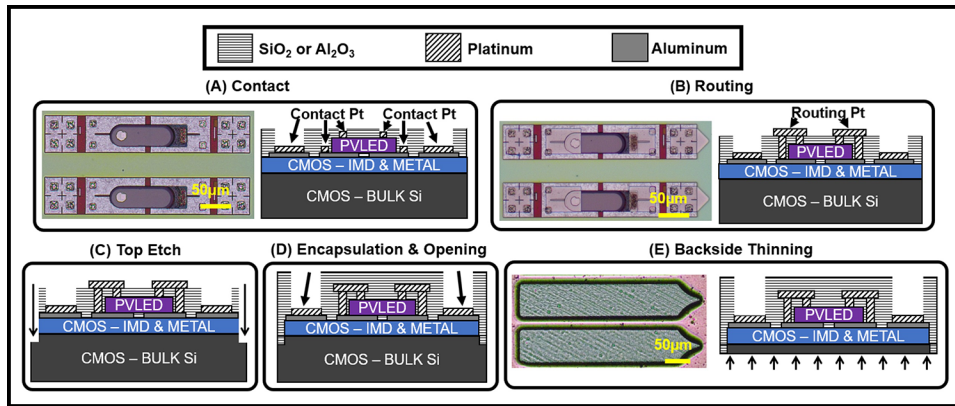


Figure 2: MOTE fabrication process. (A) An AlGaAs  $\mu$ LED (bullet-shaped) array is transferred on top of a CMOS chip containing an array of unit MOTE circuitry, and Pt is deposited over contact areas. (B) Routing Pt electrically connects each  $\mu$ LED with an underlying CMOS. (C) Each MOTE is segregated and (D) encapsulated with  $\text{SiO}_2$  and  $\text{Al}_2\text{O}_3$ , except for the measurement electrodes area. (E) The backside Si is thinned so that total thickness is  $< 30 \mu\text{m}$ . Adapted from [4].

The AlGaAs diodes are first fabricated on a sapphire wafer, to be later released from the sapphire substrate with a sacrificial poly(methyl methacrylate) (PMMA) polymer. Once the PMMA-coated AlGaAs diodes are transferred onto the CMOS die, the Oxford 81 plasma etcher is used to remove the sacrificial PMMA, leaving only the diodes array intact on the CMOS die. To establish the electrical contact between the PVLED and CMOS, we have used the CNF ABM contact aligner for photolithography with AZ nLof2020UV photoresist for efficient lift-off process that ensues after metal deposition. After the contact fabrication, the contacts of CMOS and PVLED are connected via similar photolithography process, and to maximize the conformality of the metal routing, we employ AJA sputtering. Following the routing step, each MOTE is encapsulated using Oxford ALD and PECVD for  $\text{SiO}_2$  and  $\text{Si}_3\text{N}_4$  deposition, followed by dielectric etching using OXFORD 100 and UNAXIS deep reactive ion etch (DRIE) for release. Figure 2 described the fabrication sequence described herein.

It should be noted that before embarking on the nano/micro-fabrication flow, to confirm the functionality of each module (CMOS and the diode), we use the Westbond 7400A ultrasonic wire bonder for board-level testing. ZEISS Ultra and Supra scanning electron microscopes (SEMs) are also used to inspect the fabricated MOTE for debugging purposes.

### Conclusions and Future Steps:

MOTEs are the smallest electrophysiological sensor of its kind, and we are currently testing the MOTEs *in vivo* in mouse animal models. As we accumulate more data on our ongoing *in vivo* efforts, we plan to improve fabrication processes as well as surgical procedures for inserting the MOTEs into the mouse cortex.

### References:

- [1] Harrison RR, Watkins PT, Kier RJ, Lovejoy RO, Black DJ, Greger B, and Solzbacher F. A Low-Power Integrated Circuit for a Wireless 100-Electrode Neural Recording System. *IEEE J. Solid-State Circuits*. 2006 Dec 26;42(1): 123-133.
- [2] Yang W and Yuste R. *In vivo* Imaging of Neural Activity. *Nature Methods*. 2017 Mar 31;14(4):349-359.
- [3] Lee S, Cortese AJ, Trexel P, Agger ER, McEuen PL, and Molnar AC. A  $330 \mu\text{m} \times 90 \mu\text{m}$  Opto-Electronically Integrated Wireless System-on-Chip for Recording of Neural Activities. *IEEE ISSCC*. 2018 Feb.
- [4] Lee S, Cortese AJ, Mok A, Wu C, Wang T, Park JU, Smart C, Ghajari S, Khilwani D, Sadeghi S, Ji Y, Goldberg JH, Xu C, McEuen PL, and Molnar AC. Fabrication of Injectable Micro-Scale Optoelectronically Transduced Electrodes (MOTEs) for Physiological Monitoring. *IEEE JMEMS*. 2020 June 12;29(5):720-726.

# Millimeter-Wave Large Signal Performance of AlN/GaN/AlN HEMTs

**CNF Project Number: 2800-19**

**Principal Investigator(s): Debdeep Jena, Huili Grace Xing**

**User(s): Austin Hickman, Reet Chaudhuri, Kazuki Nomoto, Lei Li**

*Affiliation(s): Electrical and Computer Engineering, Materials Science and Engineering; Cornell University*

*Primary Source(s) of Research Funding: Semiconductor Research Corporation*

*Contact(s): djena@cornell.edu, grace.xing@cornell.edu, alh288@cornell.edu*

*Primary CNF Tools Used: AFM, i-line stepper, PT770 etcher, Oxford 81 etcher, CVC SC4500 odd-hour evaporator, JEOL 6300 EBL, Oxford PECVD, AJA sputter deposition, Woollam ellipsometer, Zeiss Ultra SEM, Leica critical point dryer, Glen1000 resist stripper, P7 profilometer*

## **Abstract:**

**Gallium nitride high-electron-mobility transistors (GaN HEMTs) are ideal for high-power, gigahertz (GHz) frequency applications due to their wide bandgap and high electron saturation velocity. To further improve upon established GaN HEMTs, our group has introduced GaN HEMTs based on the aluminum nitride (AlN) platform using an AlN/GaN/AlN double heterostructure. In this report, we show the first large signal measurements for AlN/GaN/AlN HEMTs at millimeter wave frequencies (30+ GHz).**

## **Summary of Research:**

HEMTs were fabricated on the AlN/GaN/AlN heterostructure. The processing is highlighted by JEOL 6300 electron-beam lithography achieving T-gates with gate lengths as short as 60 nm. The AlN/GaN/AlN HEMTs showed on-currents over 3 A/mm and transconductance of over 0.7 S/mm. Small-signal characteristics for this device demonstrated a cutoff frequency ( $f_c$ ) and maximum oscillation frequency ( $f_{max}$ ) of 124 and 221 GHz, respectively. The HEMT was measured for large signal power sweep measurements at 30 and 94 GHz. At peak PAE, it showed associated output powers of 2.2 and 1.7 W/mm and gain of 7.1 and 3.1 dB, respectively. At peak output power, the HEMT demonstrated 2.6 and 2.2 W/mm at 30 and 94 GHz, respectively.

These numbers represent the record for HEMT on the AlN platform.

## **Conclusions and Future Steps:**

The HEMTs in this report were limited by degradation in on-current and increased gate leakage during large signal measurement. This is likely caused by the lack of a surface pretreatment before the SiN passivation, leading to excessive surface states. An additional factor could be the thicker GaN channel, which increases the stress in top barrier, leading to degradation when further stressed at high biases. Therefore, the next generation of AlN/GaN/AlN HEMTs will feature a 30 nm GaN channel to reduce stress in the barrier, and an *in situ* cleaning step to minimize surface states before SiN deposition.

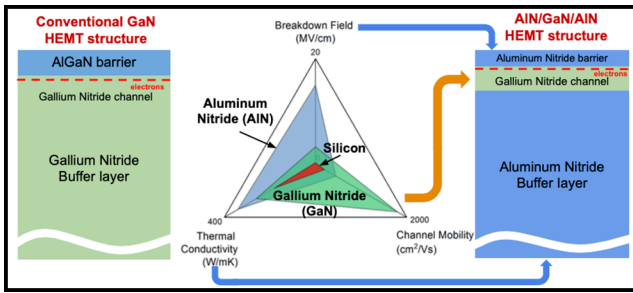


Figure 1: The cross-section of a conventional AlGaIn/GaN heterostructure (left) and our group's AlN/GaN/AlN heterostructure (right). As highlighted by the radar plot (center), the AlN/GaN/AlN heterostructure takes full advantage of what both GaN and AlN have to offer.

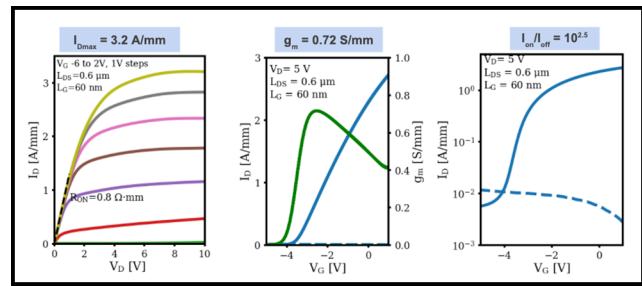


Figure 2: (left) Output characteristics of an AlN/GaN/AlN HEMT showing on-currents over 3 A/mm with high output resistance. (center) The transfer characteristics highlighted by a transconductance of 0.72 S/mm. (right) Log-scale transfer curves with an on/off ratio of  $10^{2.5}$ .

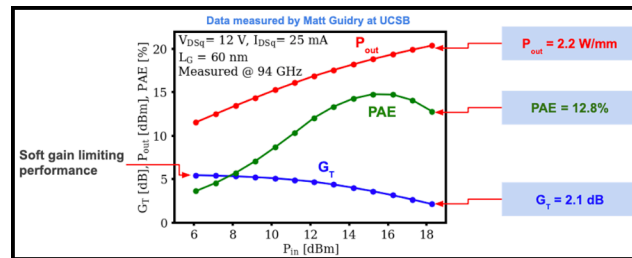


Figure 3: The load-pull power sweep of an AlN/GaN/AlN HEMT at 94 GHz. The result is highlighted by a measured output power of 2.2 W/mm.

# Nitrogen Polar III-Nitride Resonant Tunneling Diodes

**CNF Project Number: 2801-19**

**Principal Investigator(s): Huili Grace Xing, Debdeep Jena**

**User(s): Jimmy Encomendero, Yongjin Cho, Shao-Ting Ho**

*Affiliation(s): Electrical and Computer Engineering, Cornell University*

*Primary Source(s) of Research Funding: NSF*

*Contact(s): grace.xing@cornell.edu, djena@cornell.edu, jje64@cornell.edu, yc2343@cornell.edu*

*Primary CNF Tools Used: Veeco AFM, ABM contact aligner, YES asher, CVC SC4500 odd-hour evaporator, PT770 etcher, P10 and P7 profilometer, Oxford ALD, Oxford 81 etcher, AJA sputter deposition*

## **Abstract:**

We report the engineering of resonant tunneling transport in polar III-nitride heterostructures grown along the [000-1] direction of single-crystal GaN substrates. The double-barrier structures, grown by molecular beam epitaxy (MBE), consist of a 3-nm-thick GaN quantum well flanked by two 2.2-nm AlN tunneling barriers. Room temperature electronic transport reveals a peak current density of  $\sim 7.8$  kA/cm<sup>2</sup>, measured in multiple resonant tunneling diodes (RTDs) with mesa areas between 36 and 144  $\mu\text{m}^2$ . Electronic quantum interference is confirmed by the presence of repeatable room-temperature negative differential conductance (NDC) under reverse bias injection. The polarization-induced threshold voltage, characteristic in polar RTDs, is also measured at  $\sim +4.2$ V. When the devices are biased within the NDC region, microwave electronic oscillations are generated in the external circuit. Owing to the highly non-linear current-voltage characteristics, the oscillatory signal contains not only the fundamental frequency at 10.7 MHz, but also multiple harmonics up to the fifth overtone. These results constitute the first demonstration of robust resonant tunneling injection in III-Nitride N-polar RTDs capable of AC power generation.

## **Summary of Research:**

The recent demonstration of resonant tunneling transport in GaN/AlN heterostructures [1-4] has reignited interest in harnessing this quantum transport regime for the development of ultrafast high-power electronic and photonic devices. Featuring a wide and tunable band gap spanning several electron-volts, III-Nitride heterostructures stand out as a highly versatile platform for tailoring electronic states via quantum confinement. This advantage, coupled with their high breakdown electric-fields, high thermal conductivities, and high longitudinal optical (LO) phonon energies, make nitride materials a promising platform for the development of ultra-fast electronic oscillators and high-power intersubband lasers.

These new functionalities stem from the possibility of engineering ultra-fast carrier injection into discrete energy levels via resonant tunneling, thereby enabling electronic and optical gain over a wide range of frequencies. In non-centrosymmetric semiconductors, however, the engineering of quantum-confined electronic states via heterostructure design, results not only in a discontinuous energy band profile, but also generates built-in polarization charges, whose spatial distribution lacks inversion symmetry [3,5].

Therefore, in the case of Ga-polar RTDs—grown along the [0001] direction—electrons injected from the emitter side undergo enhanced quantum interference effects compared to carriers injected from the collector contact. These natural broken symmetry effects can be exploited as an additional degree of freedom for the realization of novel device functionalities. In this scenario, nitrogen-polar RTDs—grown along the [000-1] direction—offer the possibility of placing the emitter electrode on the top of the resonant tunneling structure, facilitating its integration with other materials such as ferromagnets and superconductors. Despite these advantages, N-polar RTDs have not been demonstrated so far. In this work, we report the growth, fabrication, and transport characteristics of the first N-polar GaN/AlN RTD, exhibiting robust negative differential conductance (NDC) at room temperature [5].

Molecular beam epitaxy (MBE) is employed to grow the GaN/AlN double-barrier resonant tunneling structures under metal-rich growth conditions atop a N-polar single-crystal n-type GaN substrates [6]. The structure consists of a 3 nm GaN quantum well flanked by two 2.2 nm AlN barriers that are sandwiched by heavily doped n-type GaN

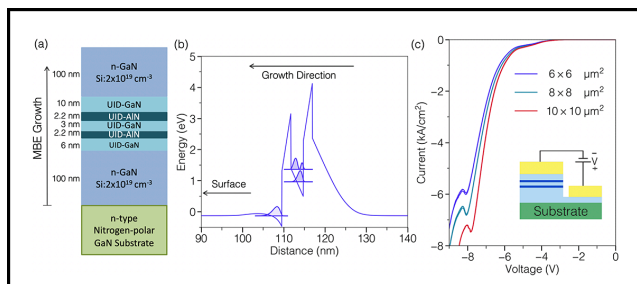


Figure 1: (a) Schematic of the nitrogen-polar RTD structure grown by molecular beam epitaxy. The structure consists of a 3 nm GaN quantum well flanked by two 2.2 nm AlN barriers that are sandwiched by heavily doped n-type GaN contact layers. (b) The band diagram of the structure shows the corresponding energies and wavefunctions of the resonant tunneling levels. (c) Current-voltage characteristics are measured at room temperature, revealing a region of negative differential conductance.

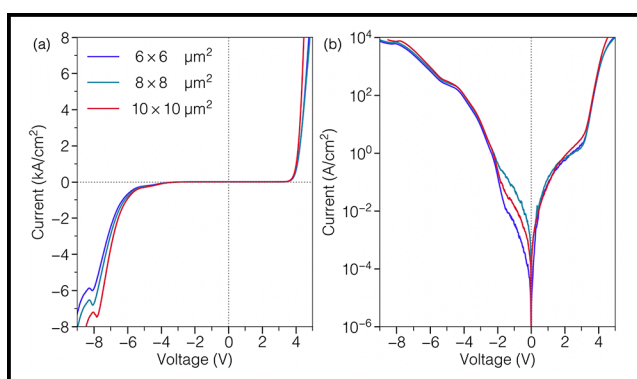


Figure 2: Electronic transport is measured at room temperature in multiple devices with different areas and under both bias polarities. (a) The linear plot shows the onset of negative differential conductance when the diode is biased at  $\sim -7.8$  V, driving a peak tunneling current of  $\sim 7.8$  kA/cm<sup>2</sup>. Under forward bias, the polarization-induced threshold voltage is measured at  $\sim +4.2$  V. (c) The logarithmic plot shows the highly asymmetric exponential modulation of the tunneling current.

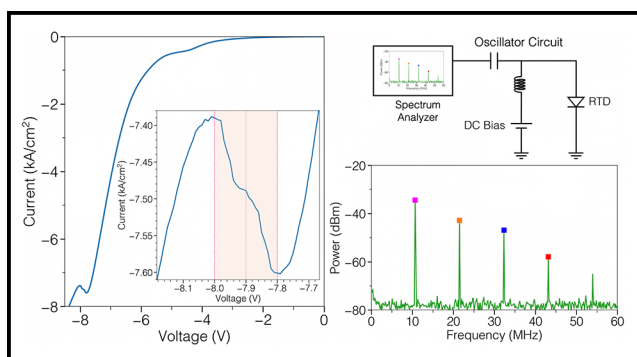


Figure 3: Nitrogen-polar RTD electronic oscillator. When the RTD is biased within the negative differential conductance (NDC) region, AC oscillations build up in the circuit. A bias tee and spectrum analyzer are employed to measure the spectrum of the AC signal. Owing to the highly non-linear characteristics of the NDC region, we measured not only the fundamental frequency at 10.7 MHz, but also multiple harmonics up to the fifth overtone.

layers. *In situ* reflection high-energy electron diffraction (RHEED) showed a  $(3 \times 3)$  surface reconstruction at low temperature after growth, indicating the conservation of the nitrogen polarity throughout the whole epitaxial process.

Sharp heterointerfaces are confirmed by the pronounced interference fringes of the symmetric X-ray diffraction (XRD) pattern. The sample also reveals smooth surface morphology with clear atomic steps. After growth, RTDs are fabricated by conventional contact lithography, reactive ion etching, and electron-beam metal evaporation.

Electronic transport is measured at room temperature, revealing negative differential conductance (NDC) due to resonant tunneling injection, in multiple devices with different mesa areas. Under reverse bias, the diodes drive a peak tunneling current of  $\sim 7.8$  kA/cm<sup>2</sup> at a resonant bias of  $\sim -7.8$  V, consistent with the energy alignment between the emitter states and the resonant level in the GaN quantum well.

Under forward bias, the polarization-induced threshold voltage is measured at  $\sim +4.2$  V. When the device is biased in the NDC-region, room-temperature electronic oscillations are generated, attesting to the robustness of the resonant tunneling phenomena [4]. Owing to the highly non-linear characteristics of the NDC region, the oscillatory signal contains not only the fundamental frequency at 10.7 MHz, but also multiple harmonics up to the fifth overtone.

These results constitute the first demonstration of robust resonant tunneling injection in III-Nitride N-polar RTDs capable of AC power generation.

## References:

- [1] J. Encomendero, et al. *Physical Review X* 7, 041017 (2017).
- [2] J. Encomendero, et al. *Applied Physics Letters* 112, 103101 (2018).
- [3] J. Encomendero, et al. *Physical Review Applied* 11, 034032 (2019).
- [4] J. Encomendero, et al. *Physical Review Applied* 13, 034048 (2020).
- [5] Y. Cho, et al. *Applied Physics Letters* 117, 143501 (2020).
- [6] J. Encomendero, et al. *Journal of Vacuum Science and Technology A* 39, 023409 (2021).

# CMOS Neural Probe with Multi-Turn Micro-Coil Magnetic Stimulation

CNF Project Number: 2847-19

Principal Investigator(s): Alyosha Molnar

User(s): Edward Szoka

Affiliation(s): Department of Electrical and Computer Engineering, Cornell University

Primary Source(s) of Research Funding: National Institute of Health

Contact(s): molnar@ece.cornell.edu, ecs227@cornell.edu

Primary CNF Tools Used: ABM contact aligner, AJA sputter deposition, Oxford 81, Oxford 100, Oxford ALD, PT770 etcher, P7 profilometer, Unaxis deep silicon etcher, Parylene coater, Westbond 7400A ultrasonic wire bonder

## Abstract:

Micro-coil magnetic stimulation has been shown to be an effective method of neurostimulation while circumventing the issues that limit the effectiveness of the more commonly used implantable electrodes [1,2]. This is due to the micro-coils not needing direct contact to the biological tissue allowing for complete device encapsulation. This allows for the stimulation effectiveness to be maintained over long periods of time while eliminating the electrode-tissue interface that is prone to electrochemical effects that can damage the probe or tissue [3]. Recent work has developed programmable micro-coil neural probes integrating complementary metal oxide semiconductor (CMOS) technology with the micro-coil design [4]. However, the design did not utilize multi-turn micro-coils to reduce the necessary stimulation current. This work proposes a neural probe that co-optimizes the micro-coil design with CMOS micro-coil current drivers to maximize the induced electric field gradients. A four-wire interface is used to supply power, deliver the stimulation current, and program the micro-coil current directions using four terminals. Preliminary *in vitro* testing with mouse olfactory bulb slices and a commercial MEA show the probes are capable of producing changes in neural behavior.

## Summary of Research:

The circuit implementation of the proposed neural probe is shown in Figure 1. A four-wire interface is implemented to reduce the number of necessary pads to power the probe, drive the micro-coils, and program the location of the stimulation sites by using the supply and differential current inputs as the programming clock and data signals respectively. The clock is generated by a comparator comparing VDD to a bias voltage. The programming data is extracted from the common-mode of the differential input current using a pair of unity gain, high output impedance amplifiers with the outputs connected together. The current drivers use a push-pull topology operating with the bias transistor pairs operating in class AB to balance between the maximum input current range and the quiescent bias current. The output of the current driver is the parallel outputs of cascoded PFET and NFET current mirrors. Cascoded outputs are used to ensure accurate current mirroring over the wide range of coil voltages present during stimulation.

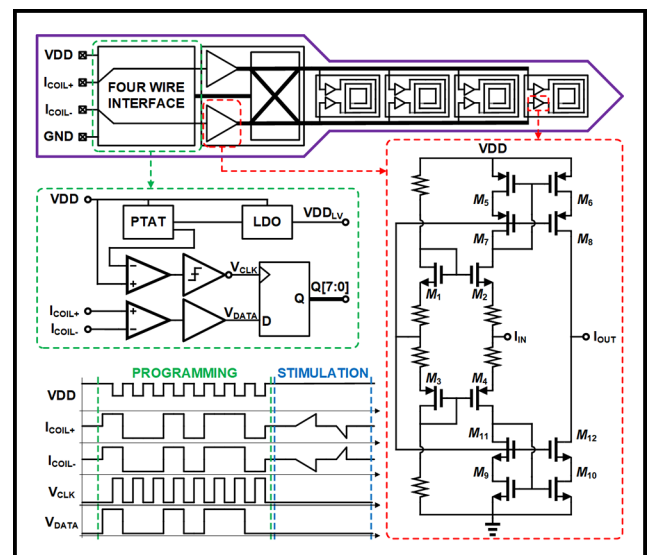


Figure 1: Circuit implementation of the proposed neural probe.

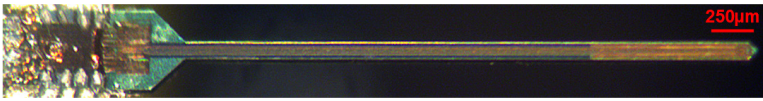


Figure 2: Micrograph of a released and fully encapsulated neural probe.

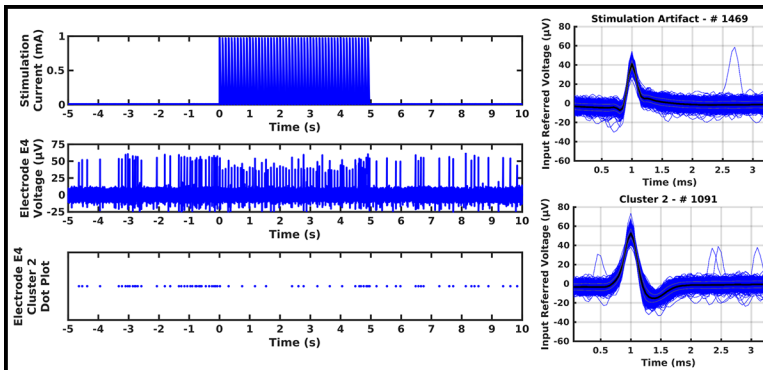


Figure 3: Preliminary data showing inhibitory neural response to stimulation train and time aligned neural spikes and stimulation artifacts.

The neural probes are thinned down and released from the original chip packaging through a series of nanofabrication steps. The neural probes are initially embedded in 5 mm × 5 mm die of foundry CMOS with a thickness of 330  $\mu\text{m}$ . Aluminum oxide and chrome are deposited (used as silicon etching and oxide etching masks respectively) and patterned using conventional photolithography and a combination of wet etching and plasma etching. The oxide is etched in a  $\text{CHF}_3/\text{O}_2$  plasma to expose the silicon surface. The exposed topside silicon is etched in a deep reactive-ion etching (DRIE) process down to the desired thickness of the neural probe of 70  $\mu\text{m}$ . The chips are flipped upside-down, and the bulk silicon is etched in the same DRIE process until the micro-coils are released from the rest of the chip. The released probes are mounted to a carrier printed circuit board using conductive silver epoxy and electrically connected using the Westbond 7400A ultrasonic wire bonder. The wire bonds are protected using a clear epoxy before the entire assembly is coated with approximately 4  $\mu\text{m}$  of Parylene-C.

*In vitro* testing is done on 300  $\mu\text{m}$ -thick mouse olfactory bulb slices with a commercial MEA. Spikes and LFPs are recorded using a 120-electrode microelectrode array with titanium nitride electrodes. The probe is placed on the surface of the slice with the micro-coils located over the region of tissue with visible activity. Testing consisted of driving the micro-coils with stimulation trains of fifty 10 Hz ramp waveforms spaced ten seconds apart while observing changes in neural behavior.

Figure 3 shows preliminary results where the micro-coils are configured to have the two inner coils run current in opposite directions to generate the strongest gradient in the electric field while the outer coils are turned off. The dot plot shows that the stimulation waveform has an inhibitory effect on the recorded activity which is consistent with the results found in [4].

### Conclusions and Future Steps:

This work proposes a neural probe that co-optimizes the micro-coil design with CMOS current drivers to maximize the electric field gradients and reduce the necessary stimulation current. Independently driven multi-turn micro-coils allow for spatially programmable neurostimulation sites between adjacent micro-coils. A four-wire interface is used to reduce the number of pads on the probe backend by using the supply and

differential current inputs as the programming clock and data signals, respectively. Preliminary *in vitro* testing of the neural probe is done with slices of a mouse olfactory bulb in conjunction with an MEA showing changes in neural behavior.

Future work looks to explore neural probe designs utilizing micro-coil magnetic stimulation with recording electrodes to allow for a closed-loop neuromodulation.

### References:

- [1] S. W. Lee, F. Fallegger, B. D. F. Casse, and S. I. Fried, "Implantable microcoils for intracortical magnetic stimulation," *Science Advances*, vol. 2, no. 12, 2016.
- [2] S. W. Lee, K. Thyagarajan, and S. I. Fried, "Micro-coil design influences the spatial extent of responses to intracortical magnetic stimulation," *IEEE Transactions on Biomedical Engineering*, vol. 66, no. 6, pp. 1680-1694, June 2019.
- [3] S. F. Cogan, K. A. Ludwig, C. G. Welle, and P. Takmakov, "Tissue damage thresholds during therapeutic electrical stimulation," *Journal of Neural Engineering*, vol. 13, no. 2, p. 021001, Jan 2016.
- [4] E. C. Szoka, J. C. Werth, S. Lee, J.-I. Lee, A. J. Cortese, T. A. Cleland, S. Fried, and A. Molnar, "Neural probe utilizing programmable microcoil magnetic stimulation," in 2021 10th International IEEE/EMBS Conference on Neural Engineering (NER), 2021, pp. 651-654.